

The overconcentrated dark halo in the strong lens SDSS J0946+1006 is a subhalo: evidence for self interacting dark matter?

Wolfgang J. R. Enzi,^{1,*} Coleman M. Krawczyk¹, Daniel J. Ballard^{1,2}, and Thomas E. Collett¹

¹ *Institute of Cosmology and Gravitation (ICG), University of Portsmouth, Burnaby Rd, Portsmouth PO1 3FX, UK*

² *Sydney Institute for Astronomy, School of Physics, University of Sydney, NSW 2006, Australia*

Accepted XXX. Received YYY; in original form ZZZ

ABSTRACT

The nature of dark matter is poorly constrained on subgalactic scales. Alternative models to cold dark matter, such as warm dark matter or self-interacting dark matter, could produce very different dark haloes on these scales. One of the few known dark haloes smaller than a galaxy was discovered in the triple source plane strong lens system J0946+1006. Previous studies have found that this structure is much more concentrated than expected in Λ CDM, but have assumed the dark halo is at the same redshift as the main deflector ($z_{\text{main}} = 0.222$). In this paper, we fit for the redshift of this dark halo. We reconstruct the first two sources in the system using a forward modelling approach, allowing for additional complexity from multipole perturbations. We find that the perturber redshift is $z_{\text{halo}} = 0.207^{+0.019}_{-0.019}$, and lower bounds on the evidence strongly prefer a subhalo over a line-of-sight structure. Whilst modelling both background sources does not improve constraints on the redshift of the subhalo, it breaks important degeneracies affecting the reconstruction of multipole perturbations. We find that the subhalo is a more than 5σ outlier from the Λ CDM $v_{\text{max}}-r_{\text{max}}$ relation and has a steep profile with an average slope of $\gamma_{2D} = -1.81^{+0.15}_{-0.11}$ for radii between 0.75 – 1.25 kpc. This steep slope might indicate dark matter self-interactions causing the subhalo to undergo gravothermal collapse; such collapsed haloes are expected to have $\gamma_{2D} \approx -2$.

Key words: gravitational lensing; strong – dark matter

1 INTRODUCTION

While Λ CDM makes successful predictions about the large-scale structure of the Universe, no particle candidate for dark matter (DM) has so far been detected in the laboratory. Although it has been studied extensively, cold dark matter (CDM) is, therefore, merely a placeholder for a more fundamental theory of dark matter. It is crucial for our understanding of astrophysics and cosmology that we place stronger constraints on its nature. The standard Λ CDM model predicts the formation of dark matter haloes that closely follow NFW mass profiles (Navarro et al. 1997). State-of-the-art hydrodynamical simulations (e.g. Schaye et al. 2015; Nelson et al. 2019; Wang et al. 2020; Hernández-Aguayo et al. 2023) indicate clear relations among the properties of these haloes, e.g. between their concentration and mass (see e.g. Sorini et al. 2024) or between the maximum circular velocity and the corresponding radius at which this velocity is found (see e.g. Moliné et al. 2023).

However, the properties of dark matter that affect galactic and subgalactic scales are still not fully constrained. Alternatives to CDM might provide a better description of structure formation on these scales. For example, Warm dark matter (WDM) would be preferred if there is a suppressed number of small mass dark matter haloes (see e.g. Bode et al. 2001; Lovell et al. 2014; Lovell 2020). Models such as fuzzy dark matter (FDM, see e.g. Hu et al. 2000; Hui et al. 2017) or self-interacting dark matter (SIDM, see e.g. Vogelsberger et al.

2012, 2016; Cyr-Racine et al. 2016; Despali et al. 2019; Yang et al. 2024) could further explain observed cores within dwarf galaxies.

SIDM is particularly interesting, as it can generate a variety of haloes with both cores and cusps. Recently, velocity-dependent SIDM became more popular since these models can create cores in small galaxies while allowing Milky way-mass haloes to remain non-spherical and therefore consistent with observations (Vogelsberger et al. 2012; Zavala et al. 2013). A SIDM halo is initially cored because the self-interaction redistributes energy and momentum mostly in the centre where most interactions occur. The core then expands as heat flows inwards from the outskirts of the halo until it becomes isothermal. This process leads to halo profiles that are less cuspy in their centre than their CDM counterparts (see e.g. Spergel & Steinhardt 2000; Shah & Adhikari 2024; Yang et al. 2024). The expansion continues until a strong enough negative energy gradient is established and the random motion of particles in the core is no longer sufficient to support its own gravity. This leads eventually to gravothermal collapse, resulting in haloes with more cuspy density profiles than their CDM cousins (see e.g. Turner et al. 2021; Yang et al. 2024). Core collapse behaves similar to the gravothermal catastrophe found in globular clusters (Lynden-Bell & Eggleton 1980).

While these alternative models make predictions that differ from CDM, the presence of baryons can also resculpt haloes without the need for exotic dark matter models (see e.g. Vegetti et al. 2023, who provide a discussion specifically in the context of gravitational lensing). Baryonic physics will further affect dark halo concentrations

* E-mail: wolfgang.enzi@port.ac.uk

(see e.g. [Heinze et al. 2024](#)) and the expected luminosity of the galaxies that they host (see e.g. [Despali et al. 2024](#)).

Strong gravitational lensing has been employed extensively to study WDM and sterile neutrinos (see e.g. [Vegetti et al. 2018](#); [Ritondale et al. 2019](#); [Gilman et al. 2020](#); [Enzi et al. 2021](#); [Nadler et al. 2021](#)), SIDM (see e.g. [Despali et al. 2022](#); [Gilman et al. 2023](#); [Kong et al. 2024](#)), and FDM (see e.g. [Powell et al. 2023](#); [Amruth et al. 2023](#)). It can be used to detect and constrain the profiles of dark haloes from their localised lensing effect on multiple images, therefore allowing us to draw conclusions on dark matter microphysics and baryonic physics. However, so far only a small number of subhalos (i.e. haloes that are hosted by more massive haloes) has been detected this way (less than five, [Vegetti et al. 2010, 2012](#); [Nierenberg et al. 2014](#); [Hezaveh et al. 2016](#)).

A particularly interesting dark perturber has been detected by [Vegetti et al. \(2010\)](#) in the lens system is J0946+1006 (which is part of the SLACS sample of lens systems, see [Gavazzi et al. 2008](#)). Previous studies of this dark halo have found it to be unusually overconcentrated ([Minor et al. 2021](#)). Recently, [Despali et al. \(2024\)](#), referred to as **D24** from here onwards) has further shown that it might further be an outlier in terms of its luminosity. [Minor \(2024\)](#), referred to as **M24** from here onwards) found that supersampling plays a significant role in the detection significance. In agreement with [Ballard et al. \(2024\)](#), referred to as **B24** from here onwards), they also find that the inclusion of the second source breaks several degeneracies in the lens model. Nonetheless, the concentration parameter remains in tension with Λ CDM.

The contributed lensing effect from line-of-sight haloes can be more important than the one from subhaloes, depending on the geometry of a lens system (see, e.g. [Despali et al. 2018](#)). If the dark halo found in J0946+1006 is a line-of-sight halo, we would expect that its redshift has important implications for the observed arcs since compound lensing can lead to qualitatively different images than single plane lensing ([Collett & Bacon 2016](#)). Only some of these effects can be absorbed by other parameters in the lens model, e.g. the mass distribution of the main deflector or the source light distribution (see e.g. [Li et al. 2017](#); [Amorisco et al. 2022](#)). We, therefore, expect to constrain the redshift of this dark halo, even though we can not directly observe its light.

So far, the redshift of this dark matter halo has not been constrained rigorously through lens modelling (although approximations have been made in the past, see, e.g. [Minor et al. 2021](#)). In this paper, we aim to constrain its redshift, test the power of compound lensing to improve these constraints, and discuss whether or not a free redshift can alleviate the observed tension with Λ CDM. Furthermore, while previous studies have not yet done so, we include the first-order multipole perturbations (the "lopsidedness") in our mass model. We infer our posteriors using the open source lens modelling code **HERCULENS**¹ ([Galan et al. 2022](#)) in combination with stochastic variational inference (SVI) and a Hamiltonian-Montecarlo-within-Gibbs sampler ([Krawczyk 2024](#)) using **NUMPYRO** ([Phan et al. 2019](#); [Bingham et al. 2019](#)).

The remainder of this paper is structured as follows. In Section 2, we describe the data that we consider for our analyses. In Section 3, we provide a brief summary on compound lensing and outline the parametric and pixelated models we use in this paper. In Section 4, we give a description of the statistical methods that we apply in this work. In Section 5, we present our results, including constraints

on the redshift of the halo, and discuss them in detail. Finally, we present our conclusions in Section 6.

2 DATA

Our analysis considers the same data as **B24**, i.e. an HST observation of J0946+1006 using the ACS in the F814W (I-band) with an exposure time of $t_{\text{exp}} = 2096$ s. This lens is part of the the SLACS sample of lenses ([Gavazzi et al. 2008](#)). Unlike **B24**, we do not subtract the lens light first, but rather model it simultaneously with the light from the sources and the mass models of the deflectors. The image has been drizzled to $0.05''$ per pixel (see [Collett & Auger 2014](#)). We model image pixels of the data shown in Figure 3, and manually create masks for the arcs of the sources allowing for no overlap. The lens system consists of a lens galaxy (which we will refer to as the main deflector) at redshift $z_{\text{main}} = 0.222$, and three sources behind it (which we will also refer to as S1, S2, and S3). These sources are located at redshifts $z_{s1} = 0.609$ ([Gavazzi et al. 2008](#)), $z_{s2} = 2.045$ (see [Smith & Collett 2021](#)), and $z_{s3} \approx 6$ (see [Collett & Smith 2020](#)).

3 STRONG GRAVITATIONAL LENS MODELLING

Below, we give a short summary of the main model components that we use throughout this work. We use **HERCULENS** and extend it for our purposes to compound lens systems. We further implement some additional lens mass profiles (see e.g. Sections 3.3.2 and 3.3.3). A diagram of our full model that we explain in the sections below is shown in Figure 1.

3.1 Single plane lensing

In this section, we provide a brief summary of the equations that describe strong gravitational lensing. In gravitational lensing, the light of a background source (here a galaxy) is deflected by some intervening mass (here other galaxies). As a result, the image plane position, \vec{x} , at which we observe the light of a source, is displaced relative to its original position in projection, $\vec{x}_{\text{source}}(\vec{x})$, by some displacement $\vec{\alpha}(\vec{x})$:

$$\vec{x}_{\text{source}}(\vec{x}) = \vec{x} - \vec{\alpha}(\vec{x}). \quad (1)$$

The lensed images, $l(\vec{x})$, depend on the both this displacement and the surface brightness of the source, $s(\vec{x})$:

$$l(\vec{x}) = s(\vec{x}_{\text{source}}(\vec{x})) = s(\vec{x} - \vec{\alpha}(\vec{x})). \quad (2)$$

Depending on the strength of the displacement, the resulting images can be highly distorted and magnified. Strong lensing occurs when the displacement is strong enough to create multiple images of the background source.

The displacement $\alpha(\vec{x})$ is related to the lensing potential, $\Psi(\vec{x})$, and convergence, $\kappa(\vec{x})$, according to:

$$\Sigma(\vec{x})/\Sigma_{\text{crit}} = \kappa(\vec{x}) = \nabla^2 \alpha(\vec{x})/2 = \nabla^2 \Psi(\vec{x})/2, \quad (3)$$

with $\Sigma(\vec{x})$ being the projected mass density of the lens and Σ_{crit} being the critical surface density. $\Sigma_{\text{crit}} = \frac{c^2}{4\pi G} \frac{D_s}{D_d D_{d,s}}$ depends on the angular diameter distances between and towards the deflector and source, that is D_d , D_s , and $D_{d,s}$. As these distances depend on cosmological parameters, we will assume $\Omega_m = 1 - \Omega_\Lambda = 0.3103$ and $h = 0.6766$ (taken from [Planck Collaboration et al. 2020](#)) in a flat Λ CDM cosmology. Calculating the displacement for a given mass distribution is equivalent to solving Equation 3 for $\alpha(\vec{x})$, usually for a given choice of the convergence, $\kappa(\vec{x})$.

¹ <https://github.com/Herculens/herculens>

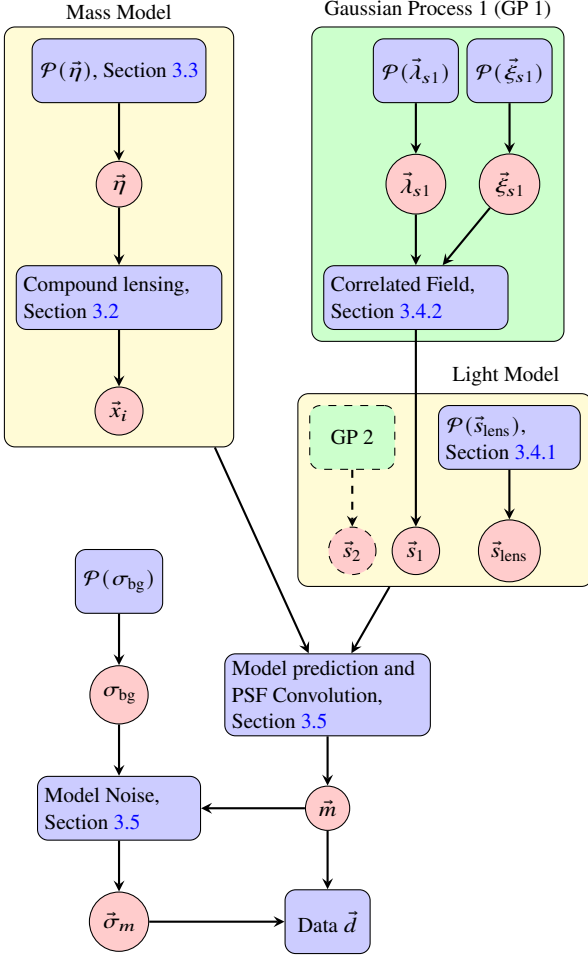


Figure 1. The model components that we consider throughout this work. We further provide the sections, in which these components are discussed in more detail. For simplicity we only show the Gaussian process (GP) that is used to model the first source in more detail. We use dashed lines to highlight that the second source is not always included.

3.2 Compound lensing

The lens system we study in this paper does not only have a single lens, but multiple galaxies that act as lenses on the sources behind them. In this compound lensing scenario, the lens equation is recursive and the projected position on the j -th redshift plane, \vec{x}_j , becomes:

$$\vec{x}_j = \vec{x}_0 - \sum_{i=1}^j \hat{\beta}_{ij} \times \alpha_{i-1}(\vec{x}_{i-1}) \text{ for } j > 0. \quad (4)$$

The parameters $\hat{\beta}_{ij}$ are related to the family ratios (see e.g. [Grillo et al. 2018](#)), and are determined from ratios of angular diameter distances between the different redshift planes:

$$\hat{\beta}_{ij} = \frac{D_{i,j} D_{i+1}}{D_i D_{i,i+1}}. \quad (5)$$

We choose $\hat{\beta}_{ij}$ such that convergences are defined relative to the next plane in redshift. We denote the sum over the images created by all the redshift planes as $l(\vec{x}_0) = \sum_{j=0}^{N_z} s_j(\vec{x}_j)$.

3.3 Mass model

3.3.1 Elliptical Power law and external Shear

We assume that to first order lenses are well described by an elliptical power law (EPL) mass profile, which we parameterize as:

$$\kappa_{\text{EPL}}(\rho, \gamma, q) = \frac{3-\gamma}{2} \left(\frac{\theta_E}{\rho} \right)^{\gamma-1}, \quad (6)$$

where $\rho^2 = x^2 q + y^2/q$ is the squared elliptical radius. We further allow the center x_c, y_c and position angle, θ , to vary freely. Rather than choosing a prior on the minor-to-major axis ratio q and position angle θ , we choose a prior on the ellipticities $\vec{e} = (e_x, e_y) = \frac{1-q}{1+q} \times (\cos(2\theta), \sin(2\theta))$ as described in [HERCULENS \(Galan et al. 2022\)](#) and [LENSTRONOMY \(Birrer & Amara 2018\)](#). In addition to this power-law mass model we allow for an external shear component, characterized by Γ_x and Γ_y . We denote the collection of EPL and Shear parameter as $\vec{\eta}_{\text{EPL}}$ and $\vec{\eta}_{\Gamma}$.

We always model the main deflector at $z_{\text{main}} = 0.222$ with an EPL with external Shear. Whenever Source 2 is included, we further model the first sources mass distribution as an singular isothermal ellipse ($\gamma = 2$), for which the center is fixed to where the average of four conjugate points is traced to on the first source plane (following [B24](#)).

3.3.2 Multipoles

To account for additional complexity in the lens, we include multipole perturbations in our model of the main deflector. We parameterize them in a way that includes the slope γ of the power-law profile and consider the orders $n \in \{1, 3, 4\}$ (implemented similar to [Powell et al. 2022](#), such that the slope is matched to the main deflector). The convergence that is associated with a given multipole is:

$$\kappa_{\mathcal{M}_n}(\rho, \gamma, a_n, \phi_n) = \kappa_{\text{EPL}}(\rho, \gamma, 1) \times A_{\mathcal{M}_n} \times \cos(n(\phi - \phi_n)), \quad (7)$$

where $A_{\mathcal{M}_n}$ is the amplitude of the n -th order multipole perturbation and ϕ_n determines its orientation (see e.g. [Chu et al. 2013](#)). Similar to the axis ratio q and position angle θ of the EPL, we do not construct our prior in terms of amplitude $A_{\mathcal{M}_n}$ and angle ϕ_n . Instead we define the multipole equivalent of ellipticities \vec{e}_n , such that $A_{\mathcal{M}_n} = 1 - q_n$ and $\phi_n = \theta_n \times 2/n$. In particular, we choose $\vec{e}_n = \frac{1-q_n}{1+q_n} \times (\cos(2\theta_n), \sin(2\theta_n))$. This ensures that the periodic boundary conditions are fulfilled, but also provides reasonable priors on the amplitudes of the multipoles.

Recent work has shown the importance of multipole perturbations to correctly recover subhaloes in lens modelling (see e.g. [Nightingale et al. 2024](#); [O’Riordan & Vegetti 2024](#)), as the additional complexity can be degenerate with the presence of dark matter haloes (in particular the \mathcal{M}_1 multipole, see e.g. [Amvrosiadis et al. 2024](#); [Lange et al. 2024](#)). Multipole perturbations have further been shown to affect the analysis of flux ratios from quasars (see e.g. [Cohen et al. 2024](#)).

3.3.3 Dark halo perturber

We assume that the perturber has a truncated NFW density profile ([Navarro et al. 1997](#)). The three dimensional NFW profile is:

$$\rho_{\text{NFW}}^{3D}(r) = \frac{\rho_s}{r_s \left(1 + \frac{r}{r_s}\right)^2}. \quad (8)$$

In projection this gives rise to a convergence of the following form (see e.g. [Keeton 2001](#)):

$$\kappa_{\text{NFW}}(r) = 2\kappa_s \frac{1.0 - F\left(\frac{r}{r_s}\right)}{\left(\frac{r}{r_s}\right)^2 - 1}, \quad (9)$$

with $r^2 = x^2 + y^2$, r_s being the scale radius of the NFW profile, and κ_s determining the amplitude of the convergence.²

We further allow the halo to be truncated at a radius r_t . We include this additional parameter to capture the effects of tidal stripping that a subhalo could experience when interacting with its host. As pointed out by [M24](#), it can further capture the virial radius at in-fall, as it would be expected to be smaller for a subhalo than for a field halo. This profile further allows easy comparison with previous works. We follow [Baltz et al. \(2009\)](#) and [Oguri & Hamana \(2011\)](#) and assume a truncated NFW profile of the following form:

$$\rho_{\text{tNFW}}^{\text{3D}}(r) = \rho_{\text{NFW}}^{\text{3D}}(r) \times \frac{r_t^2}{r_t^2 + r^2}. \quad (10)$$

The combination of all parameters that describe the perturber is referred to as η_{tNFW} . The halo center coordinates are defined relative to $x_0 = -0.68$, $y_0 = 1.0$ (or where this position is mapped to on the lens plane, if the subhalo is behind the main deflector). This position falls close to where the dark halo has been found in previous studies (see e.g. [B24](#)).

In this paper, we are interested in inferring the redshift of this dark matter halo, z_{halo} . To visualize the effects that a free redshift mass component can generate, [Figure 2](#) shows the observed light distribution of mock data for different halo redshifts in front, behind, and at the main deflector. All other parameters are kept fixed to emphasize these effects. The massive and concentrated perturber creates additional magnification and distortion in the observed arcs for all redshifts $z < z_{s1}$. Still, it will only affect the lens light if placed sufficiently far in front of it, where its lensing effect becomes efficient. We note that in practice, differences will be much smaller after lens modelling because changes in the main deflector or source light distribution can absorb some of the illustrated differences. Even so, compound lensing can generate lensed images that are qualitatively very different to those generated by single-plane lenses (see e.g. [Collett & Bacon 2016](#)).

3.4 Light model

3.4.1 Parametric lens light

We assume that the lens light can be constructed from a sum of Gaussian components (see e.g. [Shajib 2019](#); [He et al. 2024](#)), each parametrized as:

$$\mathcal{G}(\rho_n, \sigma_n) = \frac{A_n}{2\pi} \exp\left(-\frac{1}{2}\rho_n^2/\sigma_n^2\right), \quad (11)$$

where we allow the amplitudes A_n , the axis ratios q_n that appear in the radius $\rho_n = x^2 q_n + y^2/q_n$, centers and position angles to be free parameters for each component individually.

Swapping the parameters of two Gaussian components can in principle provide the same light model. To avoid additional modes in the posterior arising from this symmetry, we restrict the different Gaussian components to mutually exclusive ranges for their width σ_n .

² The expression above uses $F(x) = \tan^{-1}\left(\sqrt{x^2 - 1}\right)/\sqrt{x^2 - 1}$ for $x > 1$ and $\tanh^{-1}\left(\sqrt{1 - x^2}\right)/\sqrt{1 - x^2}$ for $0 < x \leq 1$.

The individual ranges of the $N_{\text{gauss}} = 20$ components are uniformly spaced in the logarithm of σ (similar to [Cappellari 2002](#); [Shajib 2019](#)), i.e. the range of the n -th component is defined such that $\log(\sigma_n/\sigma_{\min})/\Delta\sigma \in [n, n+1]$ with $\Delta\sigma = \frac{\log(\sigma_{\min}/\sigma_{\max})}{N_{\text{gauss}} - 1}$. We refer to the combination of all those parameters as \vec{s}_{lens} . We choose $\sigma_{\min} = 0.01$ and $\sigma_{\max} = 3.00$, which provides a good fit to the image.

3.4.2 Pixelated Sources

We assume the background sources $s(\vec{x})$ are fields that vary on regularly pixelated grids. The grid on which we reconstruct sources is fixed to the smallest square containing all the source positions corresponding to the image pixels within the masks shown in [Figure 3](#).

We assume that these fields are reasonably well described by a Gaussian process (GP). The field values in each pixel are the components of the vectors \vec{s} . For a GP, these values follow Gaussian statistics, such that in Fourier space the amplitudes are related to a power spectrum (see e.g. [Galan et al. 2022](#); [Rüstig et al. 2024](#)).

$$\vec{s} = \mathcal{F}\sqrt{P} \odot \vec{\xi}, \quad (12)$$

with each element of $\vec{\xi}$ being drawn from a zero mean unit variance Normal distribution, \odot being the pointwise multiplication, and \mathcal{F} being the Fourier transform. Following the regularization approach by ([Suyu et al. 2006](#)), the previous analysis of J0946+1006 by [B24](#) has shown that gradient regularization is preferred over curvature regularization. In this work, we want to the data to determine which regularization is used. To do so we choose a Matérn power spectrum (see e.g. [Stein 2012](#)) similar to previous works (such as [Vernardos et al. 2020](#); [Vernardos & Koopmans 2022](#); [Galan et al. 2024](#); [Rüstig et al. 2024](#)):

$$P_s(k) = \sigma^2 \times 4\pi n \left(\frac{2n}{\zeta^2}\right)^n \times \left(\frac{2n}{\zeta^2} + k^2\right)^{-(n+1)}. \quad (13)$$

The Matérn power spectrum is well-suited for a large variety of random fields. For small values of $\frac{2n}{\zeta^2}$ this power spectrum becomes similar to the more classical regularization schemes. A power spectrum of the form $P(k) = k^{-2n}$ corresponds to regularization of the n -th derivative, i.e. $n = 1$ corresponds to gradient and $n = 2$ to curvature regularization. We note that we define our power spectrum parameters in pixel units to avoid the artificial breaking of the mass sheet degeneracy. The combination of all parameters that define a source power spectrum are denoted by $\vec{\lambda} = (n, \zeta, \sigma)$.

3.5 Model observations

Our analysis includes a point-spread-function (PSF) determined from another star that lies nearby the lens in consideration (taken from [Collett & Auger 2014](#)). The noiseless model is then given by the sum of all light components (lens and lensed source images) convolved with the PSF, i.e. $m(\vec{x}) = \int d\vec{y} b(\vec{x} - \vec{y}) l(\vec{y})$. To evaluate the model $m(\vec{x})$ we use [HERCULENS](#) ([Galan et al. 2022](#)), that we extended to compound lensing (and the mass profiles as described above if they were not yet implemented). We explicitly set the source brightness to zero outside of the masks (shown in [Figures 3](#) and [5](#)) before the lensed images are being convolved. This assumption is justified, since we do not expect the sources to contribute to the observed light distribution anywhere outside of these masks. We evaluate the convolution by multiplication of the Fast Fourier Transforms of the PSF and the lensed images, while using zero-padding to avoid artifacts from periodic boundary conditions.

We include in our model the fact that different realizations of the model will give rise to different noise properties. In particular, we assume zero mean gaussian noise, \vec{n} , with a standard deviation of:

$$\vec{\sigma}_m^2 = \sigma_{\text{bg}}^2 \vec{1} + \vec{m}(\vec{\eta}, \vec{s}, z_{\text{halo}}) / t_{\text{exp}}, \quad (14)$$

thereby accounting for the fact that the noise will depend on the signal in each pixel. Here, we defined the vectors $\vec{s} = (\vec{s}_{\text{lens}}, \vec{s}_1, \vec{s}_2, \vec{\lambda}_{s1}, \vec{\lambda}_{s2})$ and $\vec{\eta} = (\eta_{\text{EPL,lens}}, \eta_{\mathcal{M}_1}, \eta_{\mathcal{M}_3}, \eta_{\mathcal{M}_4}, \eta_{\text{INFW}}, \eta_{\text{EPL,s1}})$. We infer the background noise level σ_{bg} assuming that it is drawn from a half normal distribution with a variance matching the one of background pixels in the corners of our cutout. While our data has been drizzled, we do not account for the spatially correlated noise that would result from that. For each data pixel we use a supersampling factor of four as implemented in the base version of HERCULENS. Recently, M24 has shown that this is particularly important for the detection of perturbers. We create grids with 86×86 pixels for both sources, as this provides a sufficient coverage of raytraced points per pixel.³

4 BAYESIAN INFERENCE

In the previous sections, we described all the parameters that enter our models. Below, we will first discuss the posterior, from which we aim to sample from, followed by a brief discussion of the sampling strategy we employ for this purpose.

4.1 Lens modelling posterior

The posterior from which we want to draw samples:

$$\mathcal{P}(\vec{\eta}, \vec{s}, \sigma_{\text{bg}}^2 | \vec{d}) = \frac{\mathcal{P}(\vec{d} | \vec{\eta}, \vec{s}, \sigma_{\text{bg}}) \mathcal{P}(\vec{\eta}, \vec{s}, \sigma_{\text{bg}}, z_{\text{halo}})}{\mathcal{P}(\vec{d})}. \quad (15)$$

Under the assumption of Gaussian noise the Likelihood becomes:

$$\mathcal{P}(\vec{d} | \vec{\eta}, \vec{s}, \sigma_{\text{bg}}^2) = \mathcal{G} \left(\vec{d} - \vec{m}(\vec{\eta}, \vec{s}, z_{\text{halo}}), \text{diag} \left(\vec{\sigma}_m^2 \right) \right), \quad (16)$$

where the diag operator creates a matrix with the variance in each pixel along the diagonal. In Tables 1 and 2, we report our choices of priors for the target parameters or refer to the relevant sections of this paper. While the Bayesian evidence is interesting for model comparison, we will not explicitly calculate it within this work and leave this up to future work.

We aim to obtain samples from the posterior described above. This is a challenging task because of several reasons:

(i) First of all, it is an inverse problem in the sense that we can easily model the generation of data in a forward fashion. Still, no explicit inverse function exists that returns the parameters originally entering the model that gave rise to a realization of data. Simultaneously reconstructing the source light and lens mass is also an ill-posed problem, i.e. multiple combinations thereof can give rise to the same observed data. One example of this is the well-studied Mass-Sheet Transformation (MST) or more general Source Position Transformations (Schneider & Sluse 2014). This highlights the importance of simultaneously fitting for the light and mass models to avoid artificially breaking some of these degeneracies.

³ In this context, sufficient coverage refers to the Nyquist frequency, which corresponds to the highest frequency that can be accurately recovered from a sampled signal. To achieve this we adjust grid sizes until on average two rays from the supersampled image plane trace back to each source pixel of interest.

(ii) Lens models (mainly w.r.t. the mass model, but in the case of signal dependent noise also w.r.t. the sources) are often highly non-linear. This becomes even more challenging in the case of compound lensing as shown in Equation (4). Furthermore, lens models show an intrinsic hierarchical structure, in which the source light distribution is evaluated depending on the mass distribution of the deflector. This is challenging, since hierarchies tend to generate funnel-shaped likelihoods (with a large variance in one part and an increasingly smaller variance in another part of the parameter space) that samplers can struggle with (see e.g. Neal 2000). Methods such as Slice-sampling or Gibbs sampling can alleviate such challenges.

(iii) Finally, the reconstruction of pixelated sources or lensing potentials renders lens modelling a high-dimensional problem. Accordingly, one requires sampling strategies that will not suffer from low acceptance probabilities (e.g. Hamiltonian Monte Carlo methods, HMC, Neal 2011).

4.2 Sampling strategy

To address these challenges, we employ auto-differentiable programming using the JAX-based (Bradbury et al. 2018) software HERCULENS (Galan et al. 2022) in combination with the probabilistic programming package NUMPYRO (Phan et al. 2019; Bingham et al. 2019). Our analysis follows a forward modelling philosophy, i.e. for a given set of target and nuisance parameters our model can generate simulated data according to the process shown in Figure 1. This simulated data can then be compared to real data to draw conclusions about the input parameters. Our analysis happens in two stages:

(i) We first make use of NUMPYRO's implementation of Stochastic Variational Inference (SVI, see e.g. Wingate & Weber 2013) to find an approximation to the target posterior distributions. The SVI is computationally much cheaper than Markov Chain Monte Carlo methods (see e.g. Frank et al. 2021; Galan et al. 2024) as it can make use of the auto-differentiable nature of JAX to minimize its loss function. We employ the ADABELIEF optimizer (Zhuang et al. 2020) for this purpose. We choose a low-rank multivariate Normal distribution as the guiding probability distribution, which allows to capture the main features we expect to appear in the true posterior.⁴ We incrementally allow for more complexity of the model in this step (employing parameteric sources before we move on to pixelated sources). The loss function of the SVI is the Evidence Lower Bound (ELBO), which can be used to explore different models early on in the analysis with an indication for their suitability. While the SVI is ideal for exploring different model assumptions, it tends to underestimate uncertainties, is mode seeking rather than mode covering (at least for the implementation of ELBO considered here), and is limited by the assumed shape of the approximate posterior.

(ii) To obtain more robust results, we employ the HMC-within-Gibbs sampler of Krawczyk (2024) together with the No U-Turn Sampler (NUTS, Hoffman & Gelman 2011) implemented in NUMPYRO. This setup allows us to draw samples from our posterior in a Gibbs sampling fashion (Gelman et al. 2013): we sequentially update a subset of the overall model parameters while keeping the remaining parameters fixed. This approach renders our analysis much more robust in light of the hierarchical nature of lens modelling. Similar to Gu et al. (2022), we precondition our HMC by choosing the inverse

⁴ We note that NUMPYRO performs the SVI in unconstrained spaces of the target parameters and therefore includes some coordinate transformations. This renders it possible to capture at least some non-gaussian features in the resulting SVI approximation.

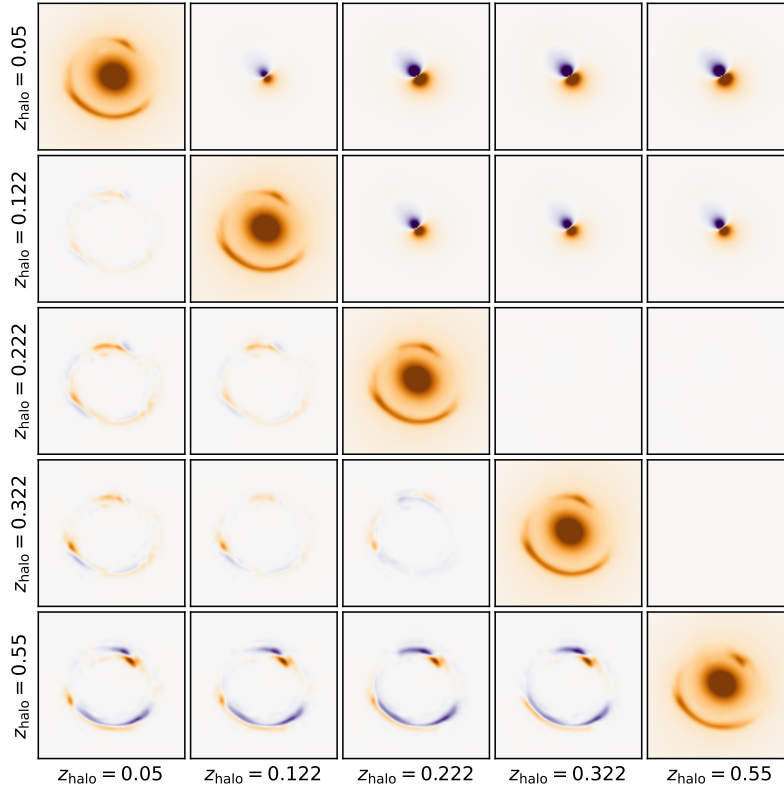


Figure 2. The effects that the subhalo redshift has on the lensed images of a background source and the main deflector light. We show five mock observations on the diagonal with halo redshifts $z_{\text{halo}} \in \{0.05, 0.202, 0.222, 0.322, 0.55\}$. All other parameters are fixed to the same values. The upper right triangle shows the differences between each combination of those mocks, considering only the light of the main deflector. The lower left triangle shows the differences between each combination of those models, considering only the resulting arcs that they generate.

covariance matrix of the SVI posterior as the initial mass matrix. We subdivide the parameters of our model into several blocks for our single (double) source models. We split our model parameters into the several subsets: $\vec{s}_{\text{lens}}, (\vec{s}_1, \vec{\lambda}_{s1}), (\vec{s}_2, \vec{\lambda}_{s2}), (\vec{\eta}_{\text{EPL,lens}}, \vec{\eta}_{\mathcal{M}_1}, \vec{\eta}_{\mathcal{M}_3}, \vec{\eta}_{\mathcal{M}_4}, \vec{\eta}_{\text{EPL,s1}}, \eta_{\text{tNFW}}, \sigma_{\text{bg}}), z_{\text{tNFW}}$. Within a single Gibbs step we subsequently sample the parameters of one of these subsets while conditioning on the remaining parameters. Sampling once over each of the conditional posteriors generates one new sample of our target posterior. The above choice of subsets ensures that our mass model is in each step sampled according to the light models.

For both the SVI and HMC-within-Gibbs step we consider 4 independent chains with different initial random seeds. We generate 20k posterior samples per chain in the second stage, each drawn after 6000 steps of warm-up. We perform analyses for both a single (S1-only) and a double source plane (S1&S2) model.

5 RESULTS AND DISCUSSION

In the following, we present the results of our analyses with the model outlined in Section 3. Figures 3, 4 and 5 show our mean reconstructed S1-only and S1&S2 models. In both cases we reconstruct the data up to the noise level. In what follows, we will discuss these results in more detail.

5.1 A main deflector with significant multipoles

We find that most main deflector parameters are compatible with the recent studies from B24 and M24, matching their parameters within 2σ . To highlight this, we show in Table 1 the number of standard deviations within which our posterior medians agree. Some larger differences appear in the external Shear and are probably explained by the inclusion of the \mathcal{M}_1 multipole, which shows the highest amplitude of all multipoles in our reconstruction with $A_{\mathcal{M}_1} = 0.036^{+0.016}_{-0.016}$ for our S1&S2 model. Since the inclusion of external shear can alleviate some deficiencies in the mass model, rather than reflecting a truly external shear (see Etherington et al. 2024), we do not expect the difference in shear to present a problem in our analysis.

Overall we find that the mass distribution of J0946+1006 is more boxy with the corners roughly aligning with those of the light distribution shown in Figure 4. This points towards the mass distribution following the lens light more closely than a simple EPL model would allow for. In agreement with He et al. (2024), we find that the lens light is very well described by a sum of Gaussian components. While the uncertainty of the lens light is higher close to the center, we find that it is strongly constrained independent of the inclusion of the second source. We, therefore, expect that our lens light subtraction is robust, which is important for the identification of dark (sub)haloes (see e.g. Nightingale et al. 2024). The orientation of Gaussian ellipses changes between the inner and outer parts of the lens light distributions. Together with the mass distributions this is characteristic for a galaxy that previously experienced a merger or interaction with another galaxy. Our constraints of $A_{\mathcal{M}_1} = 3.6$ percent are consistent

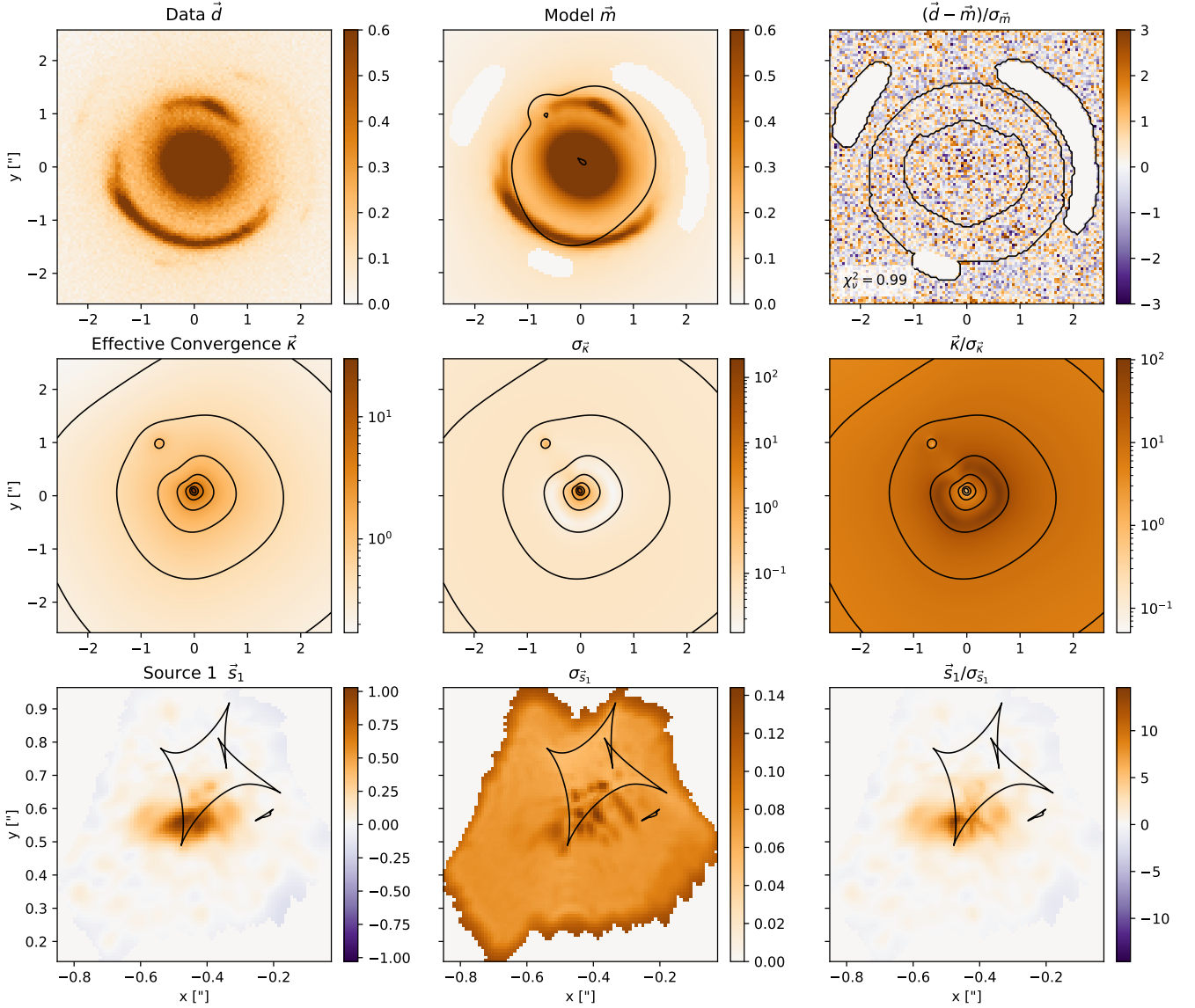


Figure 3. The mean posterior S1-only model. Shown are the original data, our model predictions, the noise-weighted residuals (row 1), the effective convergence (row 2), and the reconstructed Source 1 (row 3). The figures reporting the ratio of mean and standard deviations highlight the features most constrained by the data given our model assumptions. We also report the pixel averaged residual with χ^2_v . Note that we show the effective convergence, since the redshift of the dark halo is allowed to change during our reconstruction (see e.g. Gilman et al. 2020).

with the expectation from such interaction, which is on the order of 2 percent (at least for the light distributions of low redshift galaxies, see e.g. Amvrosiadis et al. 2024). Our inferred A_{M_1} is also similar to the one found for another lens system that has recently been studied by Lange et al. (2024), which shows $A_{M_1} = 2.4 - 9.5$ percent.

Several degeneracies exist in the posterior excluding the second source. Figure 6 shows some of the most affected posterior parameters. Notable is the strong degeneracy between the first order multipole (A_{M_1}) and the center of the main deflector. In agreement with B24, many of these degeneracies disappear with the inclusion of the second source in the model, as the arcs of the second source probe the mass distribution up to higher radii. This is not unique to compound lensing, as multiple background sources at the same redshift would also lead to additional constraints.

5.2 A very cuspy dark matter halo at the main deflector redshift

Figure 7 shows our halo redshift constraints, which for our S1-only model become $z_{\text{halo}} = 0.229^{+0.018}_{-0.015}$. The inclusion of the second source plane leads to no significant difference on the redshift uncertainty, but rather a small shift, i.e. $z_{\text{halo}} = 0.207^{+0.019}_{-0.019}$. Both posteriors point towards the halo being a subhalo. A ballpark estimate for the preference of the subhalo model over a field halo can be obtained from the ELBOs of models with and without a free redshift. Assuming each model is equally likely, the ratio of the ELBOs (corresponding to the Bayes factor α_{Bayes}) prefers a subhalo with $\log \alpha_{\text{Bayes}} \approx 8$. However, Despali et al. (2018) showed that a line-of-sight halo was a priori twice as likely as a subhalo. Putting these together, we find $\log \alpha_{\text{Bayes}} \approx 7$, corresponding to a 1 in 1000 chance of a field halo rather than a subhalo.

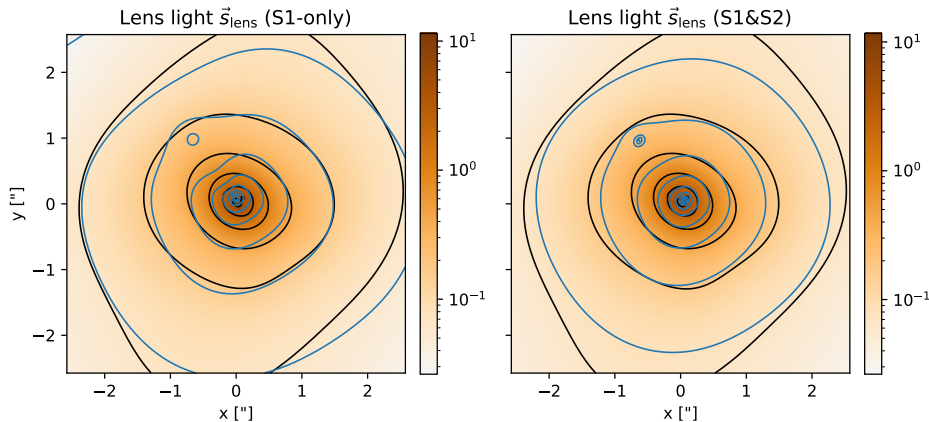


Figure 4. The reconstructed light distribution of the main deflector for our S1-only model (left) and our S1&S2 model (right). In each panel, we show the isophotes of the main deflector (black) to highlight the change in the orientation of the major axis with radius. We further include contours of the reconstructed mass distribution (blue) for comparison.

Consequently, our inferred parameters do not differ much from those found in previous studies that assume it to be a subhalo. The top right panel of Figure 6 shows the posterior of mass and concentration of the halo, which we constrain to $\log_{10} m_{200}/M_{\odot} = 9.72^{+0.17}_{-0.18}$ and $\log_{10} c_{200} = 2.55^{+0.31}_{-0.25}$. The inferred perturber would be a $\sim 4\sigma$ outlier as a field halo assuming the mass-concentration relations expected in Λ CDM extrapolated to small mass haloes.⁵ We also find that the parameters of the subhalo and main deflector do not change much with the inferred redshift value (see Figure 10) considering both their mean and standard deviations.

If the dark halo is a subhalo as expected, its properties are better characterized by relations between the maximum circular velocity, v_{max} , and the corresponding radius, r_{max} (see e.g. Molin e et al. 2017, 2023; O’Riordan & Vegetti 2024). We derive from our posterior that $v_{\text{max}} = 87.85^{+16.86}_{-9.81}$ km/s and $r_{\text{max}} = 0.28^{+0.27}_{-0.16}$ kpc with the inclusion of S2 (and $v_{\text{max}} = 97.2^{+25.7}_{-15.1}$ km/s and $r_{\text{max}} = 3.49^{+4.24}_{-2.19}$ kpc without S2). Using the relation presented by O’Riordan et al. (2023), which was based upon the ShinUchuu simulation (see Ishiyama & Ando 2020; Molin e et al. 2023), we find again that the subhalo is a $> 5\sigma$ outlier (although only 3σ when S2 is not included, see Figure 8). We note that the distribution is highly skewed towards it being more of an outlier, making a concrete statement on the level of this tension difficult due to a lack of samples close to the relation. Furthermore, the relation we use for comparison does not account for any redshift dependence.

Next, we compare our results with Λ CDM expectations from the Illustris TNG50 simulations (Pillepich et al. 2018; Nelson et al. 2019). Following Minor et al. (2021), D24, and M24, we calculate the average slope of the dark halo (within 0.75 to 1.25 kpc), γ_{2D} , and the mass it contains in projection up to 1 kpc, M_{2D} . With $\log_{10} M_{2D}/M_{\odot} = 9.61^{+0.11}_{-0.12}$ and $\gamma_{2D} = -1.00^{+0.28}_{-0.40}$ our S1-only model would also fall within the bulk of the distribution of analogous simulated haloes and not necessarily be an outlier regarding its concentration (see D24). However, including the second source, we find that $\log_{10} M_{2D}/M_{\odot} = 9.38^{+0.06}_{-0.08}$ and $\gamma_{2D} = -1.81^{+0.15}_{-0.11}$, such that the subhalo is a significant outlier. This result is in agreement

with M24, and shows the power of a compound lens for breaking modelling degeneracies.

Figure 9 shows our posterior constraints on the three-dimensional density profile of the dark halo. As seen previously, our S1&S2 model finds a much steeper profile than the one expected for an equally massive CDM halo, for which we expect $\gamma_{3D} \approx -1$ in the centre. However, with a $\gamma_{3D} \approx -3$, our density profile is in good agreement with the expectations from an SIDM core collapse scenario (Turner et al. 2021). Deviations from this power law appear only below the resolved scales, i.e. scales smaller than the full width at half maximum (FWHM) of the PSF of our HST data. This result highlights the necessity of high-resolution data to obtain stronger constraints on the density profile of this subhalo in the future. Our S1-only model shows a slope more compatible with CDM expectations, but this is an artifact of the degeneracy between substructure parameters and lens multipoles for the single plane dataset.

While the inclusion of compound lensing did not improve constraints on the redshift of the perturber, it does affect the subhalo parameters. Without the additional constraints from the second source, it is possible to have a subhalo with a larger m_{200} if the multipole perturbations adjust accordingly. Figures 3 and 5 show that this will overall keep the convergence similar.

One novel feature of our work is that we simultaneously model the lens light and the dark halo. Doing this improves our constraints on its redshift, because it rules out high mass, low redshift haloes that would also lens the main deflector light. Figure 7 shows that without this effect we would have inferred a slightly lower redshift but still compatible with a subhalo.

We further obtain the uncertainty maps $\sigma_{\vec{x}}$ of the mass distribution. We can, therefore, also see which parts of the mass distribution are the least constrained. We find higher uncertainties near the center of the main deflector and the dark halo, pointing either towards a deficiency of the chosen mass profile (of the subhalo) or the requirement of more data to constrain these parts of the mass distribution. This could be achieved, for example, by the inclusion of Muse data of the third source (Collett & Smith 2020) or the inclusion of additional data from HST or JWST imaging in various bands (see e.g. B24).

In contrast to previous works, we do not find that the truncation radius r_t is well constrained by the data. The reason for this could be the free redshift, the inclusion of the \mathcal{M}_1 multipole, or a combination of the two. With our chosen range we find that 95 percent of

⁵ Sorini et al. (2024) consider haloes down to a mass of $10^{9.5}M_{\odot}$, therefore requiring only minimal extrapolation for comparison.

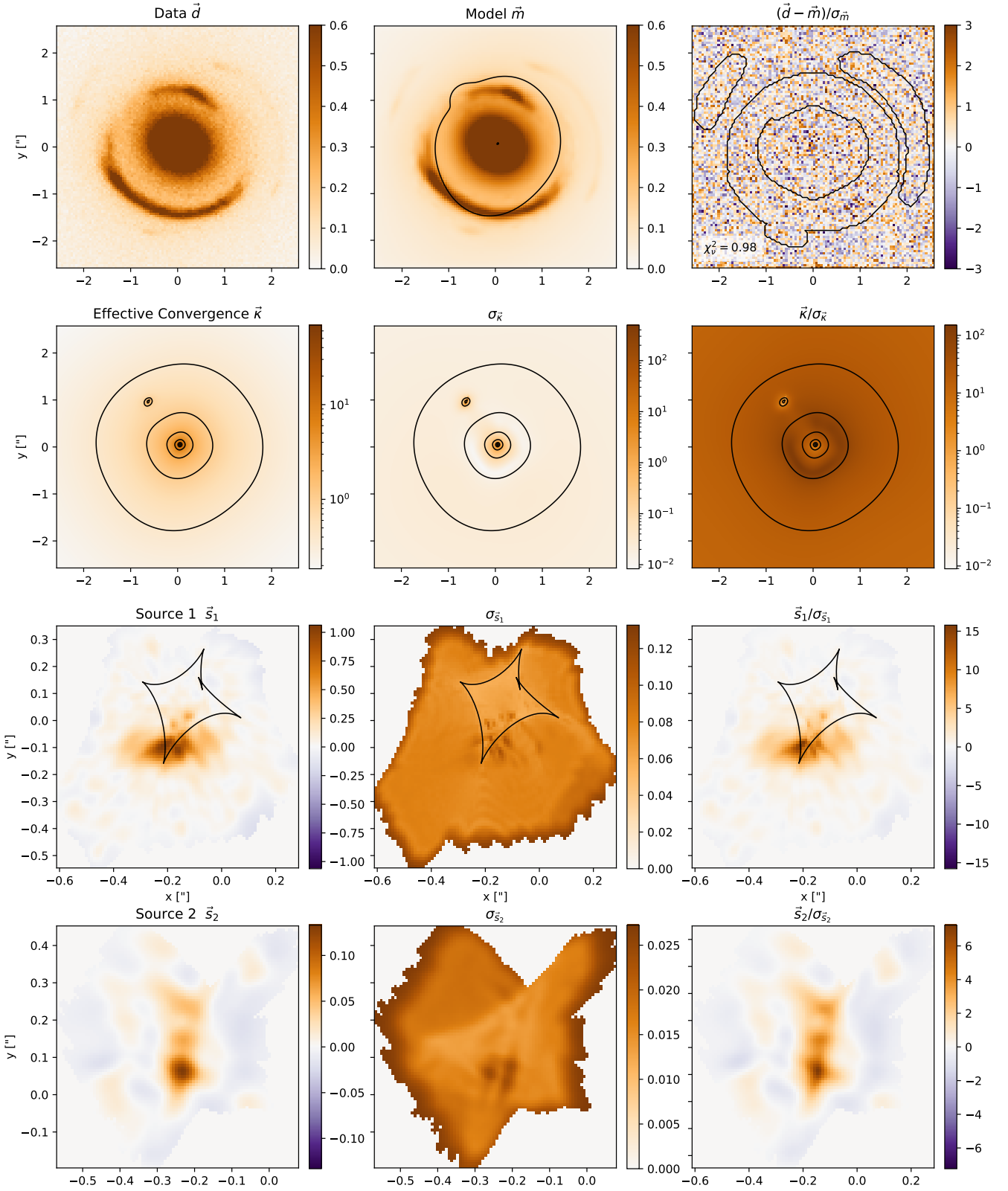


Figure 5. Same as Figure 3 but for our S1&S2 model. The second source is shown in the fourth row.

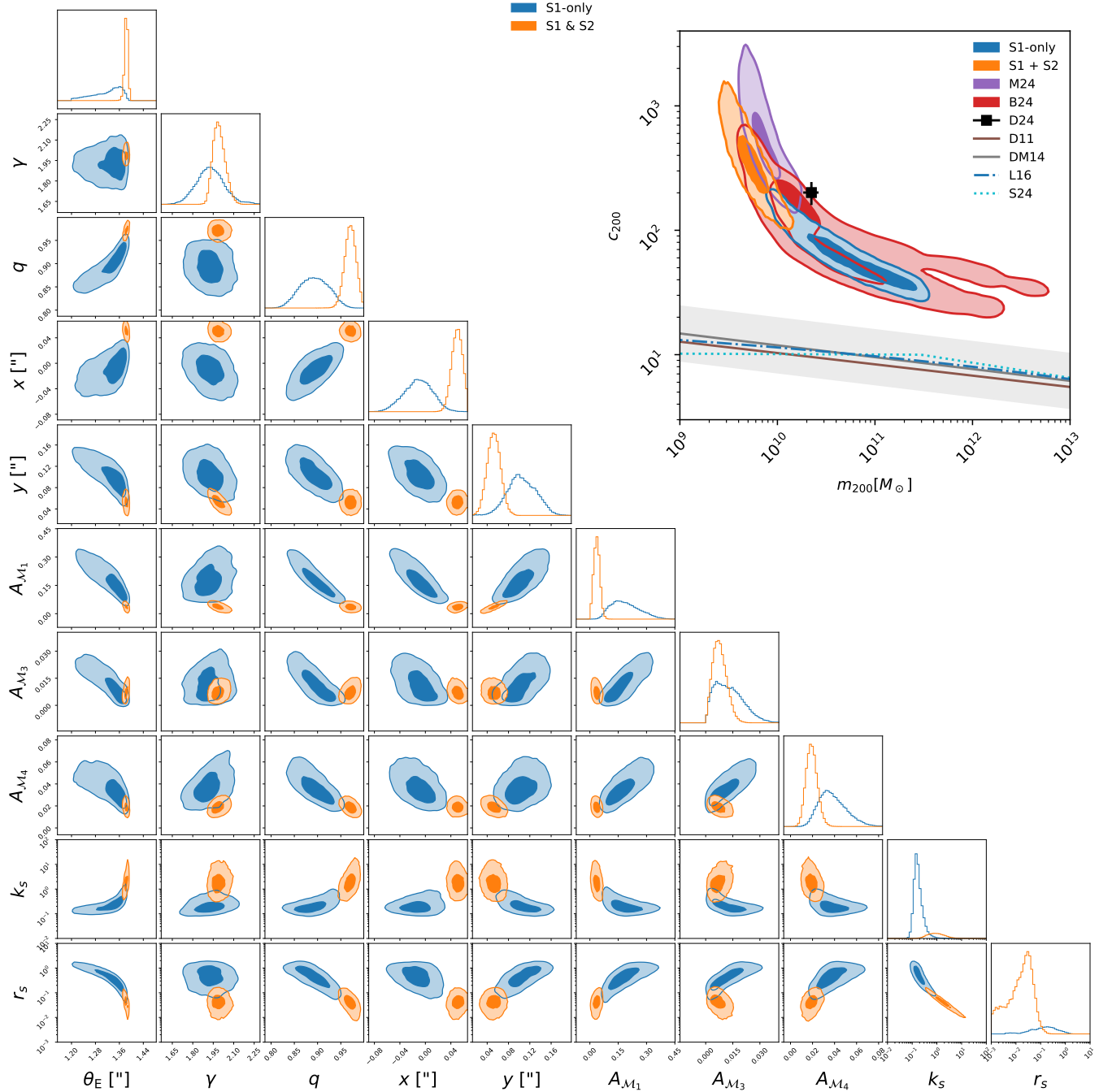


Figure 6. The 1 and 2σ posterior contours of a subset of model parameters. Blue shows our single plane model, whilst orange is the two source plane fit. The results emphasize how strongly the second source breaks model degeneracies. The top right panel further shows our posterior constraints on the mass and concentration of the dark halo, and compares to previous studies B24, D24, and M24. We further show the Λ CDM expectations from Duffy et al. (2008, D11), Dutton & Macciò (2014, DM14), Ludlow et al. (2016, L16), and Sorini et al. (2024, S24).

posterior samples fall above $r_t = 3.43''$, which is larger than the size of the data cutout we analyse in this work. We further find that the parameters r_s and r_t of the perturber are (almost) interchangeable, as the smaller one mostly decides at which point the logarithmic slope of the dark halo changes from -1 to -3 , and the larger one where it changes from -3 to -5 . One of our chains in the first source only reconstruction found a good solution with an unconstrained r_s while r_t is constrained. As pointed out by Baltz et al. (2009), a steeper cutoff might be more physically motivated for $r_t < r_s$. We therefore

do not include this chain here, even though its inclusion would not significantly change our results.

5.3 Source Reconstruction

Similar to Galan et al. (2024), we find that the GP approach can struggle with high dynamic range in the source distribution. In particular, we find that some of the star-forming regions that are present in the first source J0946+1006 appear oversmoothed in our recon-

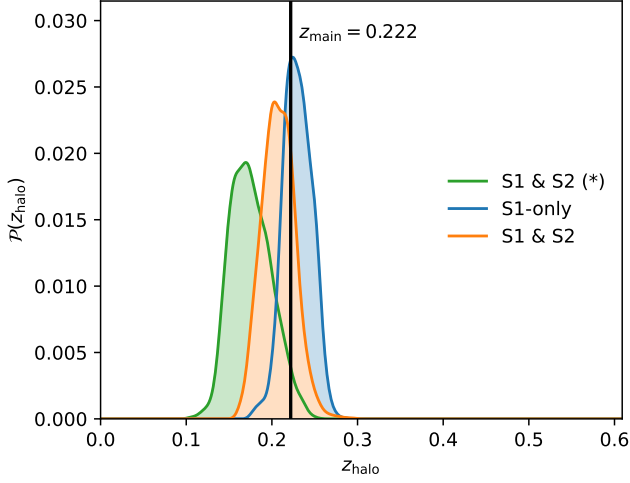


Figure 7. The posterior redshift distribution from our single source (blue) and double source (orange) lens models. The green S1 & S2 (*) shows a model where the light of the main deflector is not affected by the dark halo, even when it is in front of the lens.

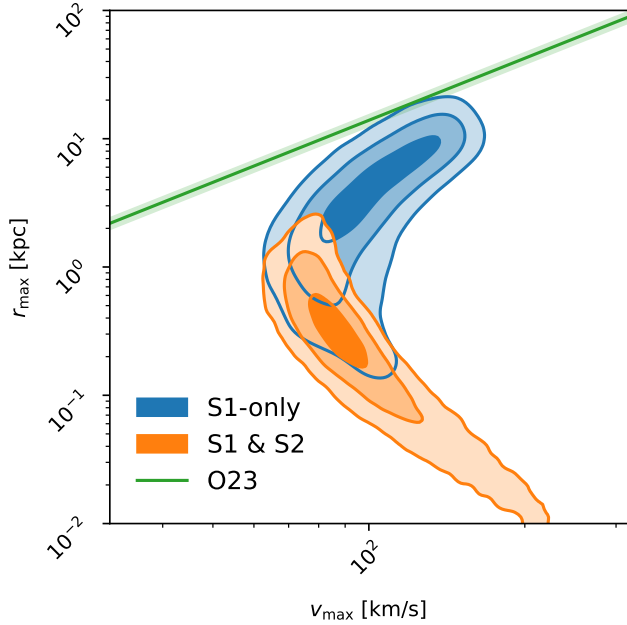


Figure 8. The first three σ contours of our posteriors on v_{\max} and r_{\max} in blue and orange. Green shows the best fit v_{\max} - r_{\max} relation derived by O’Riordan et al. (2023, O23) using the ShinUchuu simulation (Ishiyama & Ando 2020; Molin e et al. 2023). The light green shows the 2σ error of this relation (~ 10 percent).

struction. In Figures 3 and 5, we show not only the source reconstructions, \vec{s}_1 and \vec{s}_2 , but also the uncertainty maps, $\sigma_{\vec{s}_1}$ and $\sigma_{\vec{s}_2}$. Looking into the uncertainty maps, we identify multiple smaller regions of higher uncertainty. These regions could indicate how the source model struggles with the high dynamic range of features in the source, such as star-forming regions. Alternatively, this uncertainty could reflect some deficiencies in our assumed mass model. In a follow-up paper, we will consider the latter option by including

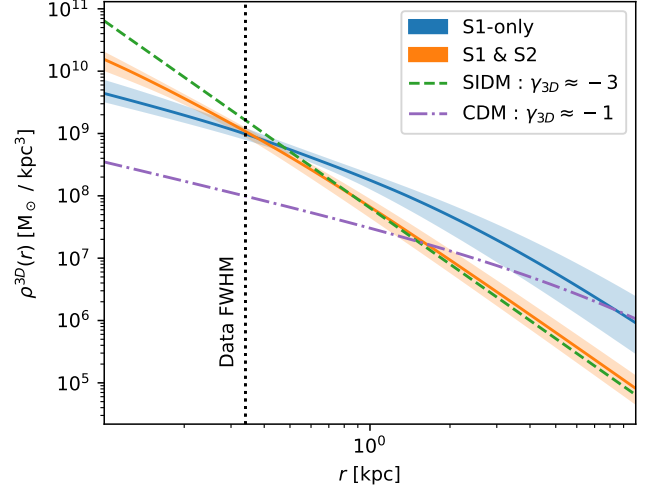


Figure 9. The reconstructed dark halo profiles for our S1-only and S1&S2 models. For comparison we show a power law with a slope of $\gamma \approx -3$ as expected for an SIDM halo (see e.g. Turner et al. 2021). We also show the expected density profile of a CDM halo with equivalent mass; the central slope should be $\gamma \approx -1$. The dotted vertical line shows the size scale that corresponds to the FWHM of the PSF (of the F814W HST data).

convergence corrections in our reconstruction. To highlight the features we reconstruct with high significance, we further show the ratio of mean and standard deviations for both sources.

Previous studies used different regularization orders of the background sources (see e.g. Vegetti et al. 2010; Ballard et al. 2024; Despali et al. 2024; Minor 2024, who used curvature and gradient, and SNR weighted regularizations). The GP approach to modelling the pixelated source allows us to be more agnostic about the correlation structure of the source or the potential corrections. In agreement with B24, we find that the first source prefers a regularization that is close to gradient regularization. Meanwhile, the second source prefers a stronger regularization on smaller scales.

6 CONCLUSIONS

In this work, we analysed the lens system J0946+1006 assuming an EPL+Shear model with multipoles and a parametric dark halo while allowing for the first time for a free redshift of the latter. Using an SVI-preconditioned HMC-within-Gibbs approach, we generate samples of posterior models that explain the data to the noise level. Our method entirely follows a forward modelling philosophy. We then discussed our results in the context of the tension that this subhalo poses for Λ CDM predictions. We summarise the conclusions of our analyses as follows:

First, the redshift of the dark structure in J0946+1006 can be constrained from its lensing effect on both the light of the main deflector and the lensed sources behind it. We find $z_{\text{halo}} = 0.207^{+0.019}_{-0.019}$, which is consistent with the main deflector redshift. A model with a subhalo is preferred with a Bayes factor of $\log \alpha_{\text{Bayes}} \approx 7$ over the field halo model. This value corresponds to posterior chance of 1 in 1000 that the halo is a field halo. The inferred values of $v_{\max} = 87.85^{+16.86}_{-9.81}$ km/s and $r_{\max} = 0.28^{+0.27}_{-0.16}$ kpc are in $> 5\sigma$ tension with the predictions from Λ CDM. If, however, the dark halo is a field halo, it would still be an $\sim 4\sigma$ outlier in Λ CDM

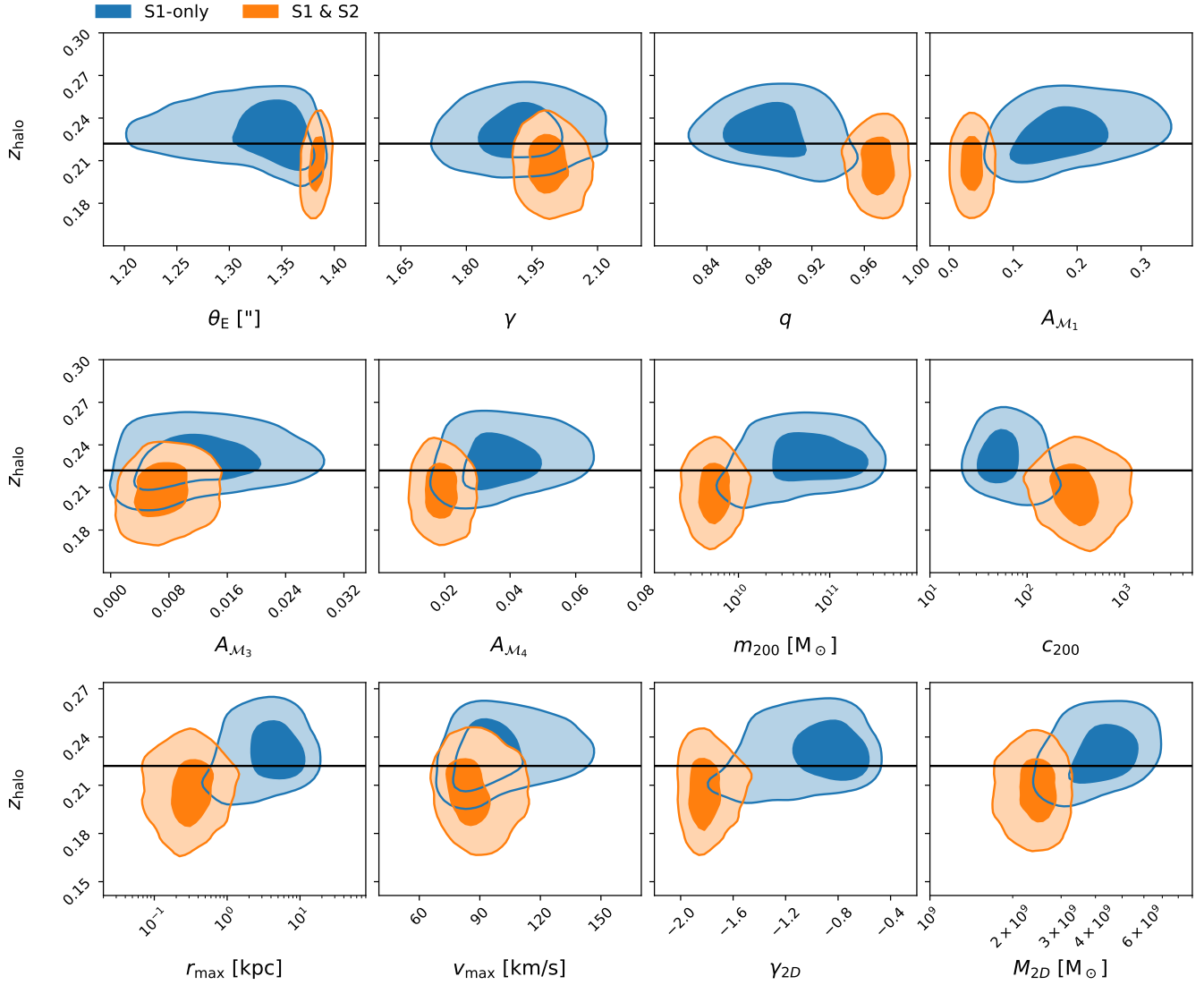


Figure 10. Projected 2D posteriors that show the (lack of) correlation between the redshift and other model parameters. The black line splits samples into those in front or behind the main deflector. The inferred parameters change only slightly with the redshift values allowed by our posterior.

given its mass, $\log_{10} m_{200}/M_{\odot} = 9.72^{+0.17}_{-0.18}$, and concentration, $\log_{10} c_{200} = 2.55^{+0.31}_{-0.25}$.

Second, compound lensing does not render the redshift constraints of the dark halo significantly more certain. However, it does help to break important degeneracies in the multipole perturbations of the main deflector. This is likely due to a larger radial coverage of the light probing the mass profile. In particular, we would expect multiple background sources at the same redshift to provide similar additional constraints on the multipoles. The additional constraints on the multipoles affect the inferred parameters describing the halo profile, e.g. its mass and concentration, but not significantly its redshift. Further degeneracies in the main deflector mass model could potentially be broken by including the kinematics of this lens (see e.g. Turner et al. 2024; Minor 2024) or additional data from other bands (see e.g. B24).

Third, the tension that this subhalo shows with respect to Λ CDM predictions deserves more attention, as it might provide a smoking gun for dark matter self-interaction. The high concentration could be explained by a core undergoing gravothermal collapse (see e.g.

Minor et al. 2021; Turner et al. 2021; Yang et al. 2024), but the existing HST data lacks the SNR or angular resolution to make such claims conclusive. In agreement with M24, we find a power law density profile slope of $\gamma_{2D} = -1.81^{+0.15}_{-0.11}$. This value is close to the $\gamma_{2D} \approx -2$ expected for gravothermally collapsed SIDM haloes (see e.g. Turner et al. 2021).

The subhalo in J0946+1006 is very much in tension with Λ CDM. In the coming years, Euclid is expected to discover $O(10^5)$ new lenses (Collett 2015) and be sensitive to 2500 subhaloes (O’Riordan et al. 2023). If the subhalo in J0946+1006 turns out to be typical, then it seems likely that CDM will soon be definitively ruled out and dark matter self-interactions preferred.

ACKNOWLEDGEMENTS

We thank Aymeric Galan, Giulia Despali, Quinn Minor, Konstantin Leyde, Dan Ryczanowski, and Andrew Gow, for the insightful discussions on several aspects of this paper. This project has received funding from the European Research Council (ERC) under the European Union's Horizon 2020 research and innovation programme (LensEra: grant agreement No 945536). TEC is funded by the Royal Society through a University Research Fellowship. Numerical computations were done on the Sciama High Performance Compute (HPC) cluster which is supported by the ICG, SEPNet and the University of Portsmouth. For the purpose of open access, the authors have applied a Creative Commons Attribution (CC BY) licence to any Author Accepted Manuscript version arising.

DATA AVAILABILITY

Supporting research data are available on reasonable request from the corresponding author and from the HST archive.

REFERENCES

- Amorisco N. C., et al., 2022, *MNRAS*, **510**, 2464
- Amruth A., et al., 2023, *Nature Astronomy*, **7**, 736
- Amvrosiadis A., et al., 2024, *arXiv e-prints*, p. [arXiv:2407.12983](https://arxiv.org/abs/2407.12983)
- Ballard D. J., Enzi W. J. R., Collett T. E., Turner H. C., Smith R. J., 2024, *MNRAS*, **528**, 7564
- Baltz E. A., Marshall P., Oguri M., 2009, *J. Cosmology Astropart. Phys.*, **2009**, 015
- Bingham E., et al., 2019, *J. Mach. Learn. Res.*, **20**, 28:1
- Birrer S., Amara A., 2018, *Physics of the Dark Universe*, **22**, 189
- Bode P., Ostriker J. P., Turok N., 2001, *ApJ*, **556**, 93
- Bradbury J., et al., 2018, JAX: composable transformations of Python+NumPy programs, <http://github.com/google/jax>
- Cappellari M., 2002, *MNRAS*, **333**, 400
- Chu Z., Lin W. P., Li G. L., Kang X., 2013, *ApJ*, **765**, 134
- Cohen J. S., Fassnacht C. D., O'Riordan C. M., Vegetti S., 2024, *MNRAS*, **531**, 3431
- Collett T. E., 2015, *ApJ*, **811**, 20
- Collett T. E., Auger M. W., 2014, *MNRAS*, **443**, 969
- Collett T. E., Bacon D. J., 2016, *MNRAS*, **456**, 2210
- Collett T. E., Smith R. J., 2020, *MNRAS*, **497**, 1654
- Cyr-Racine F.-Y., Sigurdson K., Zavala J., Bringmann T., Vogelsberger M., Pfrommer C., 2016, *Phys. Rev. D*, **93**, 123527
- Despali G., Vegetti S., White S. D. M., Giocoli C., van den Bosch F. C., 2018, *MNRAS*, **475**, 5424
- Despali G., Sparre M., Vegetti S., Vogelsberger M., Zavala J., Marinacci F., 2019, *MNRAS*, **484**, 4563
- Despali G., Walls L. G., Vegetti S., Sparre M., Vogelsberger M., Zavala J., 2022, *MNRAS*, **516**, 4543
- Despali G., Heinze F. M., Fassnacht C. D., Vegetti S., Spingola C., Klessen R., 2024, *arXiv e-prints*, p. [arXiv:2407.12910](https://arxiv.org/abs/2407.12910)
- Duffy A. R., Schaye J., Kay S. T., Dalla Vecchia C., 2008, *MNRAS*, **390**, L64
- Dutton A. A., Macciò A. V., 2014, *MNRAS*, **441**, 3359
- Enzi W., et al., 2021, *MNRAS*, **506**, 5848
- Etherington A., et al., 2024, *MNRAS*, **531**, 3684
- Frank P., Leike R., Enßlin T. A., 2021, *Entropy*, **23**, 853
- Galan A., Varnardos G., Peel A., Courbin F., Starck J. L., 2022, *A&A*, **668**, A155
- Galan A., Varnardos G., Minor Q., Sluse D., Van de Vyvere L., Gomer M., 2024, *arXiv e-prints*, p. [arXiv:2406.08484](https://arxiv.org/abs/2406.08484)
- Gavazzi R., Treu T., Koopmans L. V. E., Bolton A. S., Moustakas L. A., Burles S., Marshall P. J., 2008, *ApJ*, **677**, 1046
- Gelman A., Carlin J., Stern H., Dunson D., Vehtari A., Rubin D., 2013, *Bayesian Data Analysis*. Chapman & Hall/CRC Texts in Statistical Science, CRC Press, <https://books.google.co.uk/books?id=eSHSBQAAQBAJ>
- Gilman D., Birrer S., Nierenberg A., Treu T., Du X., Benson A., 2020, *MNRAS*, **491**, 6077
- Gilman D., Zhong Y.-M., Bovy J., 2023, *Phys. Rev. D*, **107**, 103008
- Grillo C., et al., 2018, *ApJ*, **860**, 94
- Gu A., et al., 2022, *ApJ*, **935**, 49
- He Q., et al., 2024, *MNRAS*, **532**, 2441
- Heinze F. M., Despali G., Klessen R. S., 2024, *MNRAS*, **527**, 11996
- Hernández-Aguayo C., et al., 2023, *MNRAS*, **524**, 2556
- Hezaveh Y. D., et al., 2016, *ApJ*, **823**, 37
- Hoffman M. D., Gelman A., 2011, *arXiv e-prints*, p. [arXiv:1111.4246](https://arxiv.org/abs/1111.4246)
- Hu W., Barkana R., Gruzinov A., 2000, *Phys. Rev. Lett.*, **85**, 1158
- Hui L., Ostriker J. P., Tremaine S., Witten E., 2017, *Phys. Rev. D*, **95**, 043541
- Ishiyama T., Ando S., 2020, *MNRAS*, **492**, 3662
- Jeffreys H., 1946, *Proceedings of the Royal Society of London Series A*, **186**, 453
- Keeton C. R., 2001, *arXiv e-prints*, pp astro-ph/0102341
- Kong D., Yang D., Yu H.-B., 2024, *ApJ*, **965**, L19
- Krawczyk C., 2024, CKrawczyk/MultiHMC Gibbs: v1.0.0, doi:10.5281/zenodo.12167630, <https://doi.org/10.5281/zenodo.12167630>
- Lange S. C., et al., 2024, *arXiv e-prints*, p. [arXiv:2410.12987](https://arxiv.org/abs/2410.12987)
- Li R., Frenk C. S., Cole S., Wang Q., Gao L., 2017, *MNRAS*, **468**, 1426
- Lovell M. R., 2020, *ApJ*, **897**, 147
- Lovell M. R., Frenk C. S., Eke V. R., Jenkins A., Gao L., Theuns T., 2014, *MNRAS*, **439**, 300
- Ludlow A. D., Bose S., Angulo R. E., Wang L., Hellwing W. A., Navarro J. F., Cole S., Frenk C. S., 2016, *MNRAS*, **460**, 1214
- Lynden-Bell D., Eggleton P. P., 1980, *MNRAS*, **191**, 483
- Minor Q. E., 2024, *arXiv e-prints*, p. [arXiv:2408.11090](https://arxiv.org/abs/2408.11090)
- Minor Q., Gad-Nasr S., Kaplinghat M., Vegetti S., 2021, *MNRAS*, **507**, 1662
- Moliné Á., Sánchez-Conde M. A., Palomares-Ruiz S., Prada F., 2017, *MNRAS*, **466**, 4974
- Moliné Á., et al., 2023, *MNRAS*, **518**, 157
- Nadler E. O., Birrer S., Gilman D., Wechsler R. H., Du X., Benson A., Nierenberg A. M., Treu T., 2021, *ApJ*, **917**, 7
- Navarro J. F., Frenk C. S., White S. D. M., 1997, *ApJ*, **490**, 493
- Neal R. M., 2000, *arXiv e-prints*, p. [physics/0009028](https://arxiv.org/abs/physics/0009028)
- Neal R., 2011, MCMC Using Hamiltonian Dynamics, doi:10.1201/b10905
- Nelson D., et al., 2019, *Computational Astrophysics and Cosmology*, **6**, 2
- Nierenberg A. M., Treu T., Wright S. A., Fassnacht C. D., Auger M. W., 2014, *MNRAS*, **442**, 2434
- Nightingale J. W., et al., 2024, *MNRAS*, **527**, 10480
- O'Riordan C. M., Vegetti S., 2024, *MNRAS*, **528**, 1757
- O'Riordan C. M., Despali G., Vegetti S., Lovell M. R., Moliné Á., 2023, *MNRAS*, **521**, 2342
- Oguri M., Hamana T., 2011, *MNRAS*, **414**, 1851
- Phan D., Pradhan N., Jankowiak M., 2019, *arXiv preprint arXiv:1912.11554*
- Pillepich A., et al., 2018, *MNRAS*, **473**, 4077
- Planck Collaboration et al., 2020, *A&A*, **641**, A6
- Powell D. M., Vegetti S., McKean J. P., Spingola C., Stacey H. R., Fassnacht C. D., 2022, *MNRAS*, **516**, 1808
- Powell D. M., Vegetti S., McKean J. P., White S. D. M., Ferreira E. G. M., May S., Spingola C., 2023, *MNRAS*, **524**, L84
- Ritondale E., Vegetti S., Despali G., Auger M. W., Koopmans L. V. E., McKean J. P., 2019, *MNRAS*, **485**, 2179
- Rüstig J., Guardiani M., Roth J., Frank P., Enßlin T., 2024, *A&A*, **682**, A146
- Schaye J., et al., 2015, *MNRAS*, **446**, 521
- Schneider P., Sluse D., 2014, *A&A*, **564**, A103
- Shah N., Adhikari S., 2024, *MNRAS*, **529**, 4611
- Shajib A. J., 2019, *MNRAS*, **488**, 1387
- Smith R. J., Collett T. E., 2021, *MNRAS*, **505**, 2136
- Sorini D., Bose S., Pakmor R., Hernquist L., Springel V., Hadzhiyska B., Hernández-Aguayo C., Kannan R., 2024, *arXiv e-prints*, p. [arXiv:2409.01758](https://arxiv.org/abs/2409.01758)

- Spergel D. N., Steinhardt P. J., 2000, *Phys. Rev. Lett.*, **84**, 3760
- Stein M., 2012, *Interpolation of Spatial Data: Some Theory for Kriging*. Springer Series in Statistics, Springer New York, <https://books.google.co.uk/books?id=aZXwBwAAQBAJ>
- Suyu S. H., Marshall P. J., Hobson M. P., Blandford R. D., 2006, *MNRAS*, **371**, 983
- Turner H. C., Lovell M. R., Zavala J., Vogelsberger M., 2021, *MNRAS*, **505**, 5327
- Turner H. C., Smith R. J., Collett T. E., 2024, *MNRAS*, **528**, 3559
- Vegetti S., Koopmans L. V. E., Bolton A., Treu T., Gavazzi R., 2010, *MNRAS*, **408**, 1969
- Vegetti S., Lagattuta D. J., McKean J. P., Auger M. W., Fassnacht C. D., Koopmans L. V. E., 2012, *Nature*, **481**, 341
- Vegetti S., Despali G., Lovell M. R., Enzi W., 2018, *MNRAS*, **481**, 3661
- Vegetti S., et al., 2023, *arXiv e-prints*, p. arXiv:2306.11781
- Vernardos G., Koopmans L. V. E., 2022, *MNRAS*, **516**, 1347
- Vernardos G., Tsagkatakis G., Pantazis Y., 2020, *MNRAS*, **499**, 5641
- Vogelsberger M., Zavala J., Loeb A., 2012, *MNRAS*, **423**, 3740
- Vogelsberger M., Zavala J., Cyr-Racine F.-Y., Pfrommer C., Bringmann T., Sigurdson K., 2016, *MNRAS*, **460**, 1399
- Wang J., Bose S., Frenk C. S., Gao L., Jenkins A., Springel V., White S. D. M., 2020, *Nature*, **585**, 39
- Wingate D., Weber T., 2013, *arXiv e-prints*, p. arXiv:1301.1299
- Yang D., Nadler E. O., Yu H.-B., Zhong Y.-M., 2024, *J. Cosmology Astropart. Phys.*, **2024**, 032
- Zavala J., Vogelsberger M., Walker M. G., 2013, *MNRAS*, **431**, L20
- Zhuang J., Tang T., Ding Y., Tatikonda S., Dvornik N., Papademetris X., Duncan J. S., 2020, *arXiv e-prints*, p. arXiv:2010.07468

APPENDIX A: JEFFREYS PRIOR

We employ approximations to Jeffreys prior (Jeffreys 1946) for the parameters that enter the Matern power spectrum. For the slope parameter n we find that this prior roughly follows a truncated linear distribution. We define this distribution, \mathcal{T} , on the interval $[x_{\min}, x_{\max}]$ via position x_0 , at which it intercepts the x -axis. The resulting Probability distribution is:

$$\mathcal{T}(x, x_0, a, b) = \frac{2(x - x_0)}{(x_{\max} - x_0)^2 - (x_{\min} - x_0)^2}. \quad (\text{A1})$$

We found that this is a good approximation to Jeffreys prior for the index n of the Matern kernel (within the ranges of n we consider here). For the parameter ζ , we find that Jeffreys prior is well approximated by a log-normal distribution, while the standard deviation of this power spectrum, σ , follows approximately a log-Uniform distribution. The explicit parameters that enter these distributions are shown in Table 1 and only depend very little on the number of pixels of the field (if there are more than a few).

This paper has been typeset from a $\text{\TeX}/\text{\LaTeX}$ file prepared by the author.

Table 1. This table presents the priors and posterior values of all our model parameters after the HMC stage. We refer to uniform distributions as \mathcal{U} , normal distributions as \mathcal{G} , halfnormal distributions as \mathcal{G}_+ , and the linear distribution on an interval as described in appendix A as \mathcal{T} . The agreement describes within how many standard deviations of this posterior, our reported medians match those of previous studies (rounded to the next higher integer).

| | Parameter | Prior | Posterior (Median $\pm 1\sigma$) | | Agreement within Author : $N\sigma$ |
|--------------------------------|----------------------|----------------------------|-----------------------------------|----------------------------|--|
| | | | Single Plane | Double Plane | |
| \vec{s}_{lens} | A | $10^{\mathcal{U}(-5,4)}$ | $1.9^{+3931}_{-1.9}$ | $1.3^{+3477}_{-1.3}$ | |
| | e_x | $\mathcal{G}(0, 0.1)$ | $0.001^{+0.1}_{-0.1}$ | $0.000^{+0.1}_{-0.1}$ | |
| | e_y | $\mathcal{G}(0, 0.1)$ | $0.001^{+0.099}_{-0.100}$ | $-0.001^{+0.099}_{-0.099}$ | |
| | $\sigma['']$ | Section 3.4.1 | $0.012^{+0.001}_{-0.001}$ | $0.012^{+0.001}_{-0.001}$ | |
| | $x['']$ | $\mathcal{G}(0, 0.1)$ | $-0.007^{+0.096}_{-0.13}$ | $-0.004^{+0.093}_{-0.13}$ | |
| | $y['']$ | $\mathcal{G}(0, 0.1)$ | $0.017^{+0.11}_{-0.11}$ | $0.015^{+0.11}_{-0.11}$ | |
| $\vec{\lambda}_{s1}$ | n | $\mathcal{T}(-1, 0.1, 10)$ | $0.201^{+0.094}_{-0.064}$ | $0.170^{+0.064}_{-0.047}$ | |
| | ζ | $e\mathcal{G}(2.1, 1.1)$ | $27.6^{+28.6}_{-11.6}$ | $27.3^{+28.7}_{-11.6}$ | |
| | σ | $10^{\mathcal{U}(-5,5)}$ | $0.214^{+0.034}_{-0.025}$ | $0.217^{+0.029}_{-0.022}$ | |
| $\vec{\lambda}_{s2}$ | n | $\mathcal{T}(-1, 0.1, 10)$ | - | $4.0^{+4.2}_{-3.3}$ | |
| | ζ | $e\mathcal{G}(2.1, 1.1)$ | - | $4.59^{+1.38}_{-0.87}$ | |
| | σ | $10^{\mathcal{U}(-5,5)}$ | - | $0.027^{+0.004}_{-0.003}$ | |
| $\vec{\eta}_{\text{EPL,lens}}$ | $\theta_E['']$ | $\mathcal{U}(1.2, 1.6)$ | $1.330^{+0.035}_{-0.067}$ | $1.383^{+0.005}_{-0.006}$ | B24:2, M24:2 |
| | e_x | $\mathcal{G}(0, 0.1)$ | $0.022^{+0.010}_{-0.009}$ | $0.002^{+0.004}_{-0.004}$ | |
| | e_y | $\mathcal{G}(0, 0.1)$ | $0.051^{+0.018}_{-0.018}$ | $0.014^{+0.007}_{-0.007}$ | |
| | ϕ | - | $0.579^{+0.080}_{-0.082}$ | $0.71^{+0.15}_{-0.17}$ | B24:2, M24:2 |
| | q | - | $0.893^{+0.032}_{-0.032}$ | $0.971^{+0.012}_{-0.012}$ | B24:1, M24:1 |
| | γ | $\mathcal{G}(2.0, 0.2)$ | $1.928^{+0.100}_{-0.098}$ | $1.990^{+0.049}_{-0.041}$ | B24:2, M24:2 |
| | $x['']$ | $\mathcal{G}(0.0, 0.5)$ | $-0.011^{+0.022}_{-0.023}$ | $0.050^{+0.009}_{-0.009}$ | B24:2, M24:1 |
| | $y['']$ | $\mathcal{G}(0.0, 0.5)$ | $0.104^{+0.029}_{-0.025}$ | $0.053^{+0.013}_{-0.012}$ | B24:2, M24:2 |
| $\vec{\eta}_{\Gamma}$ | Γ_x | $\mathcal{U}(-0.2, 0.2)$ | $0.057^{+0.007}_{-0.007}$ | $0.051^{+0.003}_{-0.003}$ | B24:4, M24:10 |
| | Γ_y | $\mathcal{U}(-0.2, 0.2)$ | $-0.021^{+0.008}_{-0.008}$ | $-0.039^{+0.003}_{-0.004}$ | B24:4, M24:6 |
| η_{M_1} | e_x | $\mathcal{G}(0, 0.1)$ | $0.062^{+0.037}_{-0.026}$ | $-0.003^{+0.006}_{-0.006}$ | |
| | e_y | $\mathcal{G}(0, 0.1)$ | $-0.076^{+0.030}_{-0.045}$ | $-0.017^{+0.009}_{-0.009}$ | |
| | A_{M_1} | - | $0.180^{+0.087}_{-0.067}$ | $0.036^{+0.016}_{-0.016}$ | |
| | ϕ_{M_1} | - | $-0.91^{+0.14}_{-0.12}$ | $-1.71^{+0.43}_{-0.37}$ | |
| η_{M_3} | e_x | $\mathcal{G}(0, 0.1)$ | $-0.006^{+0.004}_{-0.005}$ | $0.001^{+0.002}_{-0.002}$ | |
| | e_y | $\mathcal{G}(0, 0.1)$ | $-0.001^{+0.002}_{-0.002}$ | $0.003^{+0.002}_{-0.002}$ | |
| | A_{M_3} | - | $0.012^{+0.009}_{-0.007}$ | $0.008^{+0.004}_{-0.004}$ | B24:3, M24:2 |
| | ϕ_{M_3} | - | $-0.87^{+1.78}_{-0.11}$ | $0.39^{+0.18}_{-0.13}$ | |
| η_{M_4} | e_x | $\mathcal{G}(0, 0.1)$ | $0.013^{+0.006}_{-0.004}$ | $0.006^{+0.002}_{-0.002}$ | |
| | e_y | $\mathcal{G}(0, 0.1)$ | $-0.013^{+0.004}_{-0.005}$ | $-0.007^{+0.002}_{-0.002}$ | |
| | A_{M_4} | - | $0.037^{+0.014}_{-0.011}$ | $0.019^{+0.005}_{-0.005}$ | B24:2, M24:1 |
| | ϕ_{M_4} | - | $-0.199^{+0.030}_{-0.029}$ | $-0.216^{+0.043}_{-0.040}$ | |
| $\vec{\eta}_{\text{EPL,s1}}$ | $\theta_E['']$ | $\mathcal{U}(0, 1.0)$ | - | $0.152^{+0.038}_{-0.032}$ | |
| | e_x | $\mathcal{G}(0, 0.1)$ | - | $0.094^{+0.055}_{-0.050}$ | |
| | e_y | $\mathcal{G}(0, 0.1)$ | - | $0.109^{+0.058}_{-0.054}$ | |
| | ϕ | - | - | $0.43^{+0.21}_{-0.22}$ | |
| | q | - | - | $0.731^{+0.061}_{-0.070}$ | |
| | σ_{bg} | $\mathcal{G}_+(0.0128)$ | | $0.013^{+0.000}_{-0.000}$ | $0.013^{+0.000}_{-0.000}$ |

Table 2. Same as Table 1 but for the halo Parameters. The halos center coordinates are defined relative to $x_0 = -0.68$, $y_0 = 1.0$ (or where this position is mapped to, if the halo is behind the main deflector). We note that the compared references make different assumptions in their modelling approaches, including on the shape of the halo profile, the amount of supersampling, and the inclusion of the second source, therefore explaining some discrepancies. We also compare the halo mass with [Nightingale et al. \(2024, N24\)](#).

| | Parameter | Prior | Posterior (Median $\pm 1\sigma$) | | Agreement within Author : $N\sigma$ |
|--------------------------------------|-------------------------------|-----------------------------|-----------------------------------|----------------------------|--|
| | | | Single Plane | Double Plane | |
| $\vec{\eta}_{\text{tNFW}}$ | $\log_{10} k_s$ | $\mathcal{U}(-10, 15)$ | $-0.70^{+0.29}_{-0.16}$ | $0.30^{+0.52}_{-0.39}$ | |
| | $\log_{10} r_s'''$ | $\mathcal{U}(-10, 15)$ | $-0.38^{+0.35}_{-0.42}$ | $-1.42^{+0.29}_{-0.37}$ | |
| | $\log_{10} r_t'''$ | $\mathcal{U}(-10, 15)$ | $7.7^{+4.9}_{-5.1}$ | $7.4^{+5.2}_{-5.2}$ | |
| | $x['']$ | $\mathcal{G}(-0.3, 0.3)$ | $0.012^{+0.020}_{-0.023}$ | $0.047^{+0.018}_{-0.018}$ | |
| | $y['']$ | $\mathcal{G}(-0.3, 0.3)$ | $-0.004^{+0.028}_{-0.027}$ | $-0.029^{+0.025}_{-0.025}$ | |
| | z | $\mathcal{U}(0.001, 0.608)$ | $0.229^{+0.018}_{-0.015}$ | $0.207^{+0.019}_{-0.019}$ | |
| | $\log_{10} M_{2D}/M_{\odot}$ | - | $9.61^{+0.11}_{-0.12}$ | $9.382^{+0.064}_{-0.080}$ | M24:1 |
| | γ_{2D} | - | $-1.00^{+0.28}_{-0.40}$ | $-1.81^{+0.15}_{-0.11}$ | M24:2 |
| | $\log_{10} m_{200}/M_{\odot}$ | - | $10.69^{+0.50}_{-0.49}$ | $9.72^{+0.17}_{-0.18}$ | B24:5, M24:1, D24:4 |
| | $\log_{10} c_{200}$ | - | $1.77^{+0.27}_{-0.18}$ | $2.55^{+0.31}_{-0.25}$ | B24:3, M24:1, D24:2 |
| $\log_{10} M_{\text{tot}}/M_{\odot}$ | - | $11.52^{+0.61}_{-0.66}$ | $10.45^{+0.32}_{-0.47}$ | B24:2, M24:2, N24:5 | |
| v_{max} [km/s] | - | $97.2^{+25.7}_{-15.1}$ | $87.85^{+16.86}_{-9.81}$ | | |
| r_{max} [kpc] | - | $3.49^{+4.24}_{-2.19}$ | $0.28^{+0.27}_{-0.16}$ | | |